

# On the Impact of Additive Manufacturing Processes on the Microstructure and Magnetic Properties of Co–Ni–Ga Shape Memory Heusler Alloys

Franziska Scheibel,\* Christian Lauhoff, Stefan Riegg, Philipp Krooß, Enrico Bruder, Esmaeil Adabifroozjaei, Leopoldo Molina-Luna, Stefan Böhm, Yury I. Chumlyakov, Thomas Niendorf, and Oliver Gutfleisch


Microstructure design allows to prevent intergranular cracking and premature failure in Co–Ni–Ga shape memory alloys. Favorable grain boundary configurations are established using additive manufacturing techniques, namely, direct energy deposition (DED) and laser powder bed fusion (L-PBF). L-PBF allows to establish a columnar grain structure. In the Co–Ni–Ga alloy processed by DED, a microstructure with strong  $\langle 001 \rangle$  texture is obtained. In line with optimized microstructures, the general transformation behavior is essential for performance. Transition parameters such as transition temperature and thermal hysteresis depend on chemical composition, homogeneity, and presence of precipitates. However, these parameters are highly dependent on the processing method used. Herein, the first-order magnetostructural transformation and magnetization properties of Co–Ni–Ga processed by DED and L-PBF are compared with single-crystalline and as-cast material. In the alloy processed by L-PBF, Ga evaporation and extensive formation of the ferromagnetic Co-rich  $\gamma'$ -phase are observed, promoting a very wide transformation range and large thermal hysteresis. In comparison, following DED, the material is characterized by minor chemical inhomogeneity and transition and magnetization behavior being similar to that of a single crystal. This clearly renders DED-processed Co–Ni–Ga to become a promising candidate material for future shape memory applications.

## 1. Introduction

Ferromagnetic shape memory alloys (FMSMAs) show a large magnetic field-induced strain up to 10%,<sup>[1,2]</sup> which makes this materials interesting for magnetic actuators.<sup>[3]</sup> A promising material class for FMSMAs are Heusler alloys, such as Ni–Mn–X (X: Ga, In, Sn, Al),<sup>[2,4–8]</sup> Ni–Fe–Ga,<sup>[9]</sup> or Co–Ni–X (X: Al, Ga),<sup>[10–12]</sup> exhibiting a large shape memory effect owing to a reversible martensitic transformation. The investigated Co–Ni–Ga Heusler alloy undergoes a first-order magnetostructural transformation (FOMST) from high-temperature  $B2$ -ordered austenite to low-temperature tetragonal  $L1_0$  martensite.<sup>[13]</sup> A fully reversible superelastic response as well as excellent cyclic stability up to temperatures of 373 K has been reported for single crystals.<sup>[12]</sup> However, polycrystalline Co–Ni–Ga as well as other polycrystalline Heusler alloys suffer from intergranular cracking and premature failure after several transformation cycles due to the anisotropic volume change of randomly orientated grains.<sup>[14,15]</sup>

F. Scheibel, S. Riegg, O. Gutfleisch  
Functional Materials, Institute of Materials Science  
Technical University of Darmstadt  
Alarich-Weiss-Straße 16, 64287 Darmstadt, Germany  
E-mail: franziska.scheibel@tu-darmstadt.de

C. Lauhoff, P. Krooß, T. Niendorf  
Institute of Materials Engineering  
University of Kassel  
Moenchebergstr. 3, 34125 Kassel, Germany

 The ORCID identification number(s) for the author(s) of this article can be found under <https://doi.org/10.1002/adem.202200069>.

© 2022 The Authors. Advanced Engineering Materials published by Wiley-VCH GmbH. This is an open access article under the terms of the Creative Commons Attribution License, which permits use, distribution and reproduction in any medium, provided the original work is properly cited.

DOI: 10.1002/adem.202200069

E. Bruder  
Physical Metallurgy Division  
Institute of Material Science  
Technical University of Darmstadt  
Alarich-Weiss-Straße 2, 64287 Darmstadt, Germany

E. Adabifroozjaei, L. Molina-Luna  
Advanced Electron Microscopy  
Institute of Materials Science  
Technical University of Darmstadt  
Alarich-Weiss-Straße 2, 64287 Darmstadt, Germany

S. Böhm  
Institute for Production Technologies and Logistics  
University of Kassel  
Kurt-Wolters-Str. 3, 34125 Kassel, Germany

Y. I. Chumlyakov  
Siberian Physical Technical Institute  
Tomsk State University  
Novosobornay Square 1, 634050 Tomsk, Russia

Efforts in the fields of grain boundary engineering and direct microstructure design have been carried out to realize FMSMAs with favorable grain boundary configurations to fully prevent intergranular cracking and premature failure.<sup>[16–18]</sup> For example, in Cu-based SMAs, the structural and functional limitations could be overcome by a columnar microstructure with strong (001) texture and straight, low-angle grain boundaries.<sup>[19–21]</sup>

For Co–Ni–Ga alloys, a highly anisotropic microstructure, that is, columnar grained and in some cases even strongly textured, could be realized using additive manufacturing, namely, laser powder bed fusion (L-PBF) and direct energy deposition (DED).<sup>[22–24]</sup> During the L-PBF process, prealloyed powder is molten layer by layer utilizing a laser system operating under inert gas atmosphere to prevent oxidation. The microstructure can be directly tailored by choice of suitable processing parameters like laser power, hatch spacing, layer thickness, or scanning speed and strategy.<sup>[24–26]</sup> In contrast to the L-PBF process, DED is a powder spraying-based process using nozzles to directly transfer the material powder into a focused laser beam, the latter being collinear with spraying direction. Similar to the L-PBF process, the microstructure can be directly designed by employing adequate processing parameters like laser power, focus distance, or material and gas flow. Owing to the strongly textured and columnar grained microstructure, additive manufactured Co–Ni–Ga obtained by DED shows excellent functional properties without conducting any postprocessing heat treatment.<sup>[23]</sup>

However, improving the structural integrity of FMSMAs by tailoring the microstructure also affects the transformation behavior during the magnetic–structural phase transition. In Heusler alloys like Co–Ni–Ga, the FOMST depends on several parameters including grain size, texture, secondary phases, defects, and atomic ordering.<sup>[27–33]</sup> Figure 1 depicts

schematically the interrelationships between microstructural features, that is grain size, texture and chemical composition (precipitates, chemical inhomogeneity, evaporation losses), the transition temperature  $T_t$ , transition width, and thermal hysteresis  $\Delta T_{\text{hyst}}$  for Co–Ni–Ga Heusler alloys. Furthermore, the composition also determines the saturation magnetization  $M_{\text{sat}}$  and the Curie temperature  $T_C$ . An increase in  $T_C$  and  $M_{\text{sat}}$  can result from higher Co content, due to the higher magnetic moment of the Co atoms.<sup>[27,34]</sup>

Defects can reduce  $T_C$  but also lead to an increase in  $T_t$  due to the stabilization of the martensite.<sup>[33,35]</sup> Furthermore, the FOMST of Co–Ni–Ga is strongly dependent on the chemical composition.  $T_t$  increases with increasing valence-electron-to-atom ratio ( $e/a$ ). The  $e/a$  ratio can be increased by substitution of Ga by Ni or Co by Ni or Ga by Co.<sup>[30,32,34,36–38]</sup>  $T_t$  and  $M_{\text{sat}}$  are also affected by the formation of secondary phases ( $\gamma$  and  $\gamma'$ -phase), as their formation changes the chemical composition in the surrounding matrix ( $\beta$ -phase).<sup>[17,27,39–41]</sup> The formation of  $\gamma'$ -phase is observed after annealing between 623 and 873 K,<sup>[39,42,43]</sup> while the formation of  $\gamma$ -phase is observed after annealing at higher temperatures between 973 and 1473 K.<sup>[27,40,44]</sup>

In the present work, microstructure and magnetic properties of Co–Ni–Ga alloys processed by L-PBF and DED are compared with single-crystalline and polycrystalline cast material to determine the influence of the processing method and microstructure on the FOMST. For this, detailed microstructure analysis was carried out using high-resolution scanning electron microscopy (HR-SEM) and transmission electron microscopy (TEM). FOMST and magnetic properties were investigated using temperature-dependent magnetization measurements. This method is very sensitive to changes in magnetization or changes in

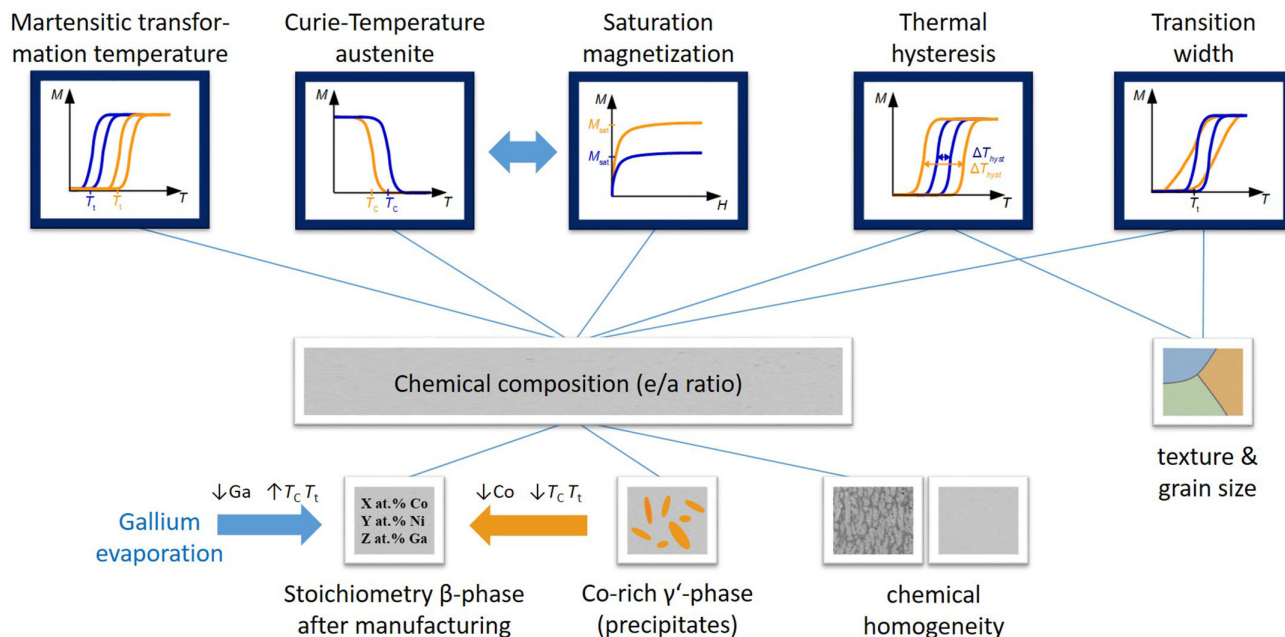


**Figure 1.** Schematic illustrating the correlation between chemical composition as well as grain size and texture and the functional and magnetic properties, that is, transitional temperature  $T_t$ , Curie temperature  $T_C$ , thermal hysteresis  $\Delta T_{\text{hyst}}$ , as well as the transition width and saturation magnetization  $M_{\text{sat}}$  in the Co–Ni–Ga system.

phase. Therefore, determination of FOMST and  $M_{\text{sat}}$  by temperature-dependent magnetization measurements in combination with isothermal magnetization measurements can provide information on chemical composition, homogeneity, and microstructure. Major differences were found regarding the magnetic properties, especially the transition width and  $\Delta T_{\text{hyst}}$  of the FOMST; in addition, interrelationships between the microstructural features and the FOMST are established.

## 2. Experimental Section

In this study, Co–Ni–Ga FMSMA processed by different techniques was investigated. The Co–Ni–Ga alloy with a nominal chemical composition of  $\text{Co}_{49}\text{Ni}_{21}\text{Ga}_{30}$  (in at. %) was obtained in form of polycrystalline ingots in the as-cast condition (Sophisticated Alloys, USA). The composition was designed for improved functional properties featuring a high degree of strain recoverability.<sup>[45]</sup> Using the as-cast ingots, single crystals were grown by the Bridgman technique under He atmosphere. For characterization of the functional properties, thin plates of 0.5 mm thickness were electrodischarge machined (EDM) from the bulk single crystals such that lateral edges were parallel to the  $\langle 001 \rangle$  crystal direction of the austenite, while the lateral surfaces were normal to  $\langle 001 \rangle$ . Following mechanical grinding to remove the EDM-affected surface layer, the plates were used in their as-grown state for microstructural and functional characterization.

For studies on the influence of different microstructures, the Co–Ni–Ga FMSMA was additively manufactured by two different techniques, namely, L-PBF and DED. For fabrication, spherical-shaped Co–Ni–Ga powder<sup>[22]</sup> was obtained by gas atomization of the as-cast material carried out by TLS Technik (Bitterfeld, Germany). Its chemical composition was double checked using energy-dispersive X-Ray spectroscopy (EDS), conforming the same composition as the as-cast material ( $\text{Co}_{49}\text{Ni}_{21}\text{Ga}_{30}$ ), within the accuracy of the EDS technique. Powder material with an average particle size  $< 20 \mu\text{m}$  was processed by DED on a 773 K preheated Co–Ni–Ga substrate material. The powder was fed to the jet nozzle with a rate of  $16.8 \text{ g min}^{-1}$ . Argon was used as carrier gas as well as shielding gas to prevent oxidation. A 2 kW multi-mode fiber laser with a wavelength of 1070 nm (YLS-2000-S2, IPG Photonics) and an operating power of 400 W was used to deposit a Co–Ni–Ga structure (with dimensions of  $40 \times 30 \times 3.5 \text{ mm}^3$ ) on the cobalt substrate using a quasi bidirectional scanning strategy. For more details on the DED setup and the processing parameters used, the reader is referred to other studies.<sup>[23,46]</sup> For L-PBF processing, a SLM280<sup>HL</sup> (SLM Solutions, Luebeck, Germany) using a 400 W laser was used. Cuboidal blocks ( $10 \times 10 \times 15 \text{ mm}^3$ ) were manufactured using powder material with a particle size ranging from 20 to 52  $\mu\text{m}$ , layer thickness of 50  $\mu\text{m}$ , and a hatch distance of 0.12 mm. The processing was done under argon atmosphere on a base plate heated to 773 K. The laser was operated at a nominal power of 250 W and a scan velocity of  $700 \text{ mm s}^{-1}$ . A bidirectional scanning strategy with  $90^\circ$  rotation between the successive layers was applied. In the remainder of the text, the building direction (BD) was the direction perpendicular to the building platform. The chemical compositions determined by EDS of all material conditions are shown in Table 1. For microstructure analysis

**Table 1.** Chemical composition and valence-electron-to-atom ratio (e/a) of the Co–Ni–Ga samples produced by casting (as-cast), additive manufacturing using DED and L-PBF, and the Bridgman technique (single crystal). the compositions were determined via EDS point analysis (see text for details).

Sample	Co [at. %]	Ni [at. %]	Ga [at. %]	e/a ratio
As-cast	48.9	21.0	30.1	7.40
DED	49.9	20.7	29.4	7.44
L-PBF	50.7	21.1	28.2	7.52
Single crystal	50.0	21.1	28.9	7.48

scanning electron microscopy (SEM) including electron backscatter diffraction (EBSD) was used employing a TESCAN CamScan MV 2300 microscope. EDS analysis was conducted using an EDAX Octane Plus detector and a Tescan Vega 3 SEM. HR-SEM images were acquired using a TESCAN MIRA3-XMH SEM equipped with a four-quadrant solid-state backscattered electron (BSE) detector from DEBEN. All measurements were performed at room temperature. Samples were mechanically ground down to a grit size of 5  $\mu\text{m}$  and vibration polished for 2.5 h using a 0.02  $\mu\text{m}$  colloidal  $\text{SiO}_2$  polishing suspension.

The lamellae for TEM investigations were prepared conventionally using mechanical polishing and argon-ion milling (precision ion polishing system [PIPS]; Gatan Dual Ion Mill Model 600). The milling was done at an angle of  $7^\circ$  and an energy of 4 keV for 2 h, while cooling the sample was realized using liquid nitrogen. Scanning transmission electron microscopy (STEM) was conducted using a Jeol JEM 2100 F STEM equipped with an Oxford X-max80 EDX detector operating at 200 kV. Temperature and field-dependent magnetization measurements in the temperature range between 200 and 450 K were performed utilizing a LakeShore 7410 vibrating sample magnetometer (VSM) with a 2 T field. For the low-temperature range between 10 and 200 K, a Quantum Design Physical Properties Measurement system (PPMS) with a 9 T field and VSM insert was used.

## 3. Results and Discussion

### 3.1. Microstructure and Chemical Composition of Additively Manufactured Co–Ni–Ga Compared with Polycrystalline as-Cast Material and Single Crystals

To evaluate the magnetic properties of the samples processed by different additive manufacturing techniques, the composition and microstructure had to be correlated with single-crystalline as well as polycrystalline as-cast material. Figure 2 shows results obtained by EBSD for the following three material conditions: Figure 2a) as-cast, additive manufactured by Figure 2b) L-PBF and Figure 2c) DED, respectively. The results are illustrated as color-coded grain maps (color coding is indicated in the standard triangle in Figure 2d) accompanied by the corresponding inverse pole figures (IPFs). All samples are in the austenite state, and the EBSD was indexed with a B2 cubic crystal structure ( $Pm\bar{3}m$ ) and

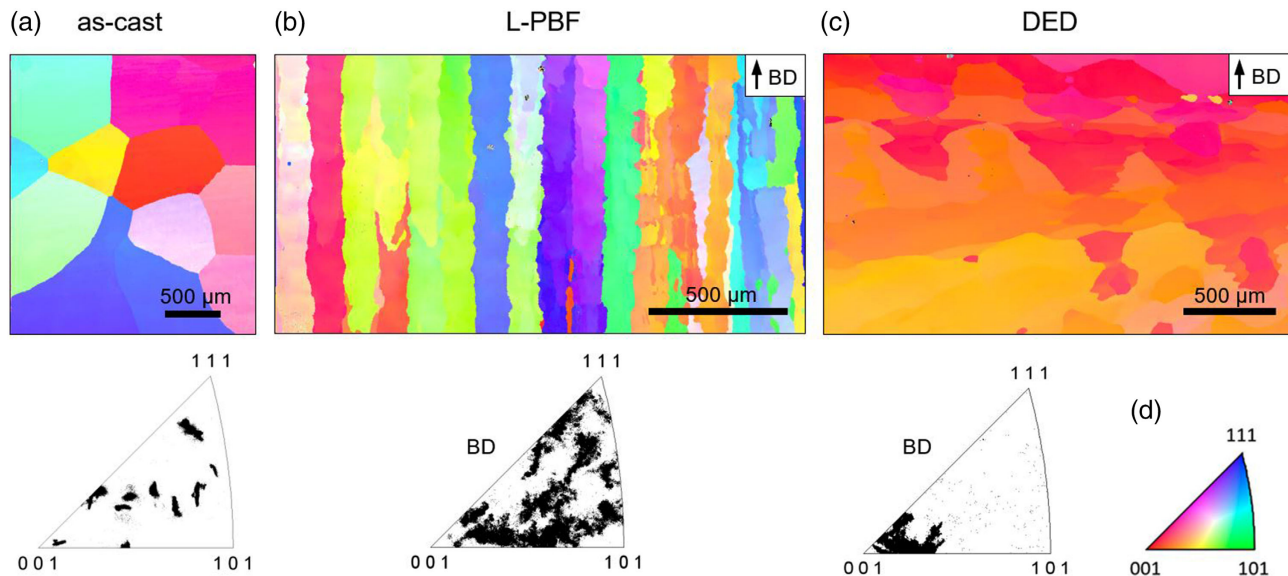


**Figure 2.** Room temperature EBSD analysis of Co–Ni–Ga in polycrystalline a) as-cast, b) L-PBF, and c) DED-processed condition. EBSD IPF mappings and IPFs are plotted with respect to the out-of-plate direction (as-cast) and the BD (L-PBF and DED). The BD is indicated by arrows; the color-coded standard triangle is shown on the right side (d).

a lattice parameter of  $a = 0.2287$  nm. The samples differ in average grain size and texture. The sample in the as-cast condition (Figure 2a) is characterized by a polycrystalline structure with no preferred crystallographic orientation and an average grain size of  $\approx 1$  mm. The microstructure is comparable with that of previous studies.<sup>[14,15]</sup> The microstructure of the L-PBF-processed sample (parallel to the BD) is shown in Figure 2b. The microstructure is dominated by columnar grains growing parallel to the BD, and the grains have a length of several millimeters and a width of  $\approx 100$   $\mu\text{m}$ . The EBSD IPF plot calculated with respect to the BD does not reveal a distinct texture. However, Figure 2b shows that texture can certainly be observed within a single column; this is caused by epitaxial grain growth along the BD. During L-PBF processing, previous layers of the material are partially remelted, leading to epitaxial solidification. The strong columnarity and the epitaxial growth along the BD have been reported in previous study.<sup>[22]</sup> In contrast to the previous work,<sup>[22]</sup> process-related defects were avoided in the L-PBF sample shown here by heating the build plate to 773 K. Previously reported DED-processed Co–Ni–Ga samples show a strong near- $\langle 001 \rangle$  texture along the BD and excellent superelasticity.<sup>[23]</sup> DED process parameters used here are the same as in the aforementioned study and, thus, a highly anisotropic microstructure with a strong  $\langle 001 \rangle$  texture along the BD is present as well (Figure 2c). The texture along the BD can be achieved by choosing adequate process parameters for favorable epitaxial solidification, but this also depends on the manufacturing process itself. For cubic materials such as Co–Ni–Ga, the  $\langle 001 \rangle$  direction is the preferred growth direction along the maximum thermal gradient,<sup>[47]</sup> that is, for the DED process along the BD.

The chemical composition and the  $e/a$  ratio of the polycrystalline as-cast, additively manufactured (L-PBF and DED), and the single-crystalline samples are shown in Table 1. The compositions were determined via EDS (point analysis, spot size

1–2  $\mu\text{m}$ , accuracy of 1 at%). The values in Table 1 represent the average calculated from 14-point spectra. Apart from the different particle size distributions, the same batch of powder material obtained from the as-cast alloy (see Experimental Section) was used for both additive manufacturing techniques. Consequently, the deviation of the chemical composition between the additively manufactured Co–Ni–Ga and the as-cast condition reveals that (considering the applied process parameters in both cases) during L-PBF processing an amount of 1.9 at% Ga evaporated, while the DED process only caused a loss of 0.7 at% Ga. For the single-crystalline material, a loss of 1.2 at% is observed. The  $e/a$  ratio increases with decreasing Ga content and therefore also affects  $T_t$ , which will be discussed in detail later.

Detailed microstructural investigations were performed by HR-SEM. BSE images in Figure 3 depict the L-PBF ((a) and (b)) and DED ((c) and (d)) samples. For the L-PBF sample (Figure 3a), a columnar grain structure along the BD is visible, as already seen in the EBSD IPF map in Figure 2b. The high-magnification micrograph presented in Figure 3b reveals that the L-PBF condition is characterized by the presence of needle-like shaped precipitates with a length of 50–400 nm and a width of 5–25 nm. The darker contrast indicates that the precipitates contain a higher content of Co than the surrounding matrix. This is confirmed by STEM–EDS. Figure 4a shows a bright-field (BF) TEM image of the L-PBF sample with the same needle-like shaped structure detailed before. The BF STEM image in Figure 4b highlights two precipitates (dark phases) surrounded by the Co–Ni–Ga matrix (bright phase). The EDS line scan (Figure 4c) across these two precipitates (dark contrast within the TEM image of Figure 4b) reveals a higher Co concentration in the precipitates compared with the surrounding matrix. The higher Co concentration as well as the needle-like shape point in the presence of  $\gamma'$ -precipitates. In literature, this

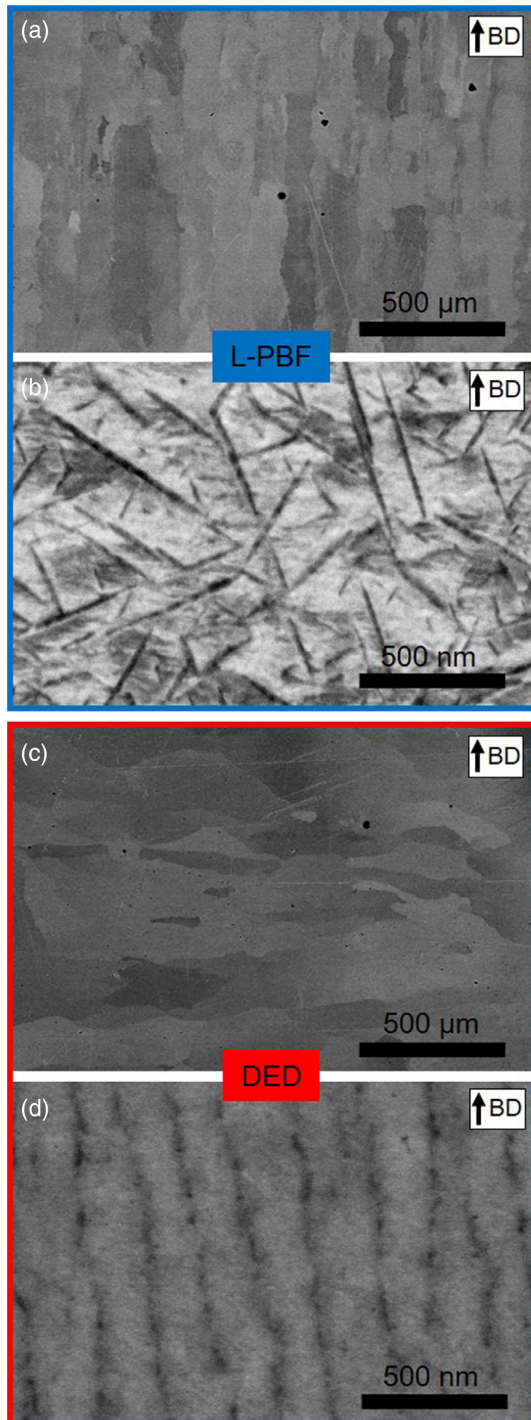


**Figure 3.** HR-SEM analysis showing BSE images of a,b) L-PBF and c,d) DED-processed Co–Ni–Ga. The BD is indicated by arrows. Images were acquired at room temperature.

nanometric secondary phase is reported to occur mainly in reannealed Co–Ni–Ga alloys at temperatures between 623 and 873 K. The  $\gamma'$ -phase exhibits higher Co content than the surrounding  $\beta$ -phase matrix and elongated or needle-like shapes close to the equilibrium condition.<sup>[40,43,48,49]</sup> In present work, the formation

of  $\gamma'$ -phase can be most likely attributed to the elevated built temperature of 773 K during processing. Although the DED sample was processed using the same elevated built temperature, BSE images in Figure 3c,d do not reveal any needle-like shaped precipitates. Instead, a stripe-like structure is seen alongside the BD (Figure 3d). Here, the difference in contrast indicates a variation in chemical composition. STEM–EDS was also performed on the DED sample (not shown). However, the stripe-like structure in Figure 3d could not be resolved, the effect will be subject of future investigations. The differences in the microstructure, that is, precipitation of the  $\gamma'$ -phase and chemical inhomogeneity in the L-PBF and DED-processed Co–Ni–Ga samples, respectively, can be attributed to the different thermal profiles during additive manufacturing processing. In both processes, an elevated built temperature of 773 K was selected; however, the dwell time/build time of the L-PBF sample is higher than that of the DED sample by a factor of 10. In addition, in the L-PBF process, the sample is always in thermal contact with the powder bed, while in the DED process, the sample is fabricated free standing. Therefore, the evolution of equilibrium phases (Figure 3a,b and 4) can be observed in the L-PBF sample, while the chemical segregation patterns in the DED sample (Figure 3c,d) are thought to be related to the epitaxial solidification along the BD.

### 3.2. Magnetic Characterization

Figure 5 depicts the results of the temperature-dependent magnetization  $M(T)$  measurements of Co–Ni–Ga in Figure 5a) the single-crystalline and Figure 5b) polycrystalline as-cast, DED-, and L-PBF-processed state. The measurements were performed under isofield conditions in a magnetic field of 0.05 T. In case of the single crystal, the  $M(T)$  curve is measured for three different orientations: (001), (011), and (111) axis parallel to the external magnetic field (Figure 5a). The single crystal is characterized by a  $T_C$  of 387 K. At temperatures above  $T_C$ , the paramagnetic (PM) austenitic state ( $B2$  crystal structure) is present, while below  $T_C$ , the magnetic moments order ferromagnetically (FM), and the crystal structure remains  $B2$  (austenite). At  $\approx 256$  K, the crystal undergoes a FOMST from FM austenite to FM martensite during cooling. The reverse transformation upon heating from the martensite to austenite phase is observed at 276 K. A  $\Delta T_{\text{hyst}}$  of the FOMST is observed. The comparison of the  $M(T)$  curves for the different crystal orientations shows no variation of  $T_C$ . Furthermore,  $T_i$  of the FOMST,<sup>[50]</sup> namely, austenite and martensite start ( $A_S$ ,  $M_S$ ) and finish temperatures ( $A_F$ ,  $M_F$ ), and  $\Delta T_{\text{hyst}}$  are the same within the range of the experimental error. The austenite and martensite start ( $A_S$ ,  $M_S$ ) and finish temperatures ( $A_F$ ,  $M_F$ ) were determined by the tangent method,<sup>[51]</sup>  $\Delta T_{\text{hyst}}$  and  $T_C$  were determined by the maximum and minimum of the derivative  $dM(T)/dT$ . All characteristic temperatures for the three crystal directions are listed in Table 2 and will be discussed later in more detail. The different magnetization values in the FM austenitic and martensitic state above and below the FOMST (s. Figure 5a) can be explained by the relatively low applied field of 0.05 T. In this low field, the magnetization of the crystal is not saturated and, thus, varies between individual  $M(T)$  measurements depending on the magnetization history details.

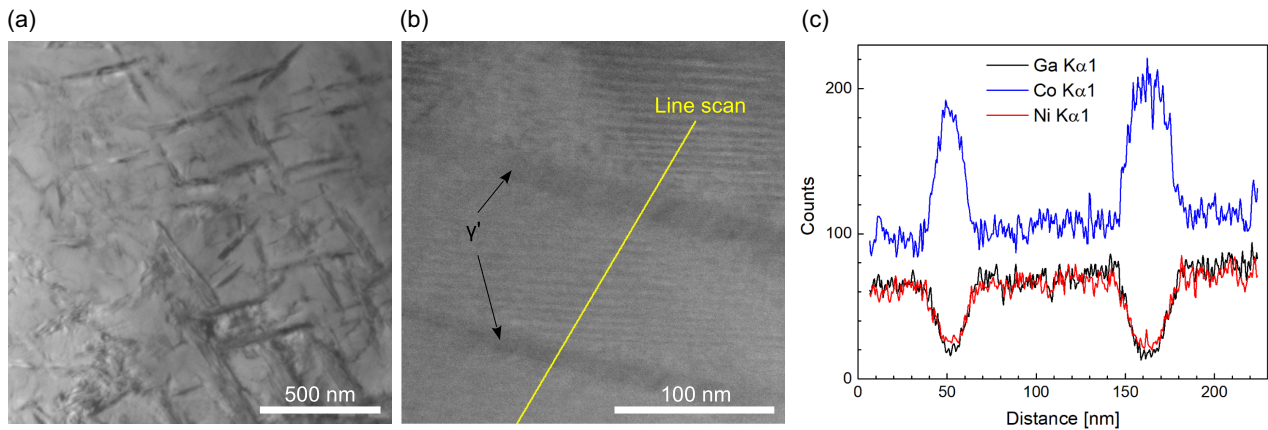


**Figure 4.** TEM analysis of L-PBF processed Co-Ni-Ga: a) BF-TEM image, b) BF-STEM image of two needle-like shaped precipitates embedded in the Co-Ni-Ga matrix, and c) STEM-EDS line scan across the two precipitates showing Co-rich  $\gamma'$ -precipitates. Images were acquired at room temperature.

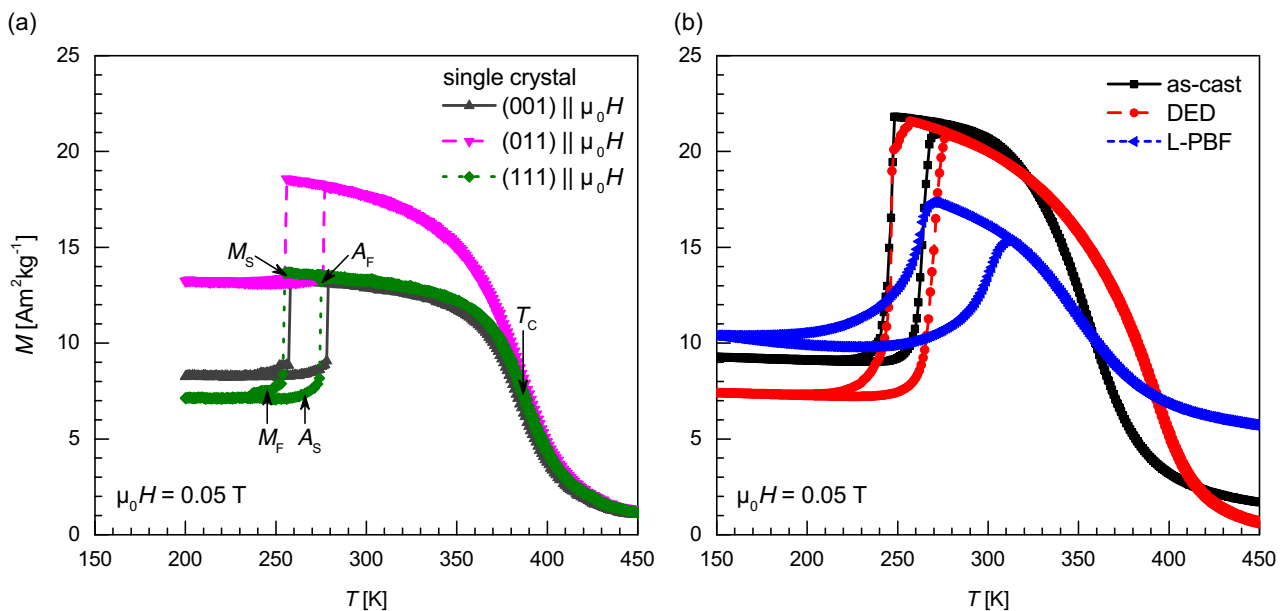


**Figure 5.** Temperature-dependent magnetization of a) single-crystalline Co-Ni-Ga with the orientations of (001), (011), and (111) parallel to the external magnetic field, and b) polycrystalline Co-Ni-Ga in as-cast, DED-, and L-PBF-processed state. In case of the DED- and L-PBF-processed samples, the magnetic field is applied parallel to the BD. All measurements were performed in a magnetic field of 0.05 T.

The  $M(T)$  curves of the as-cast, DED, and L-PBF samples are depicted in Figure 5b. All samples exhibit a magnetic transition from PM to FM austenite in the range  $348 \text{ K} < T_C < 388 \text{ K}$  and a FOMST from austenite to martensite in the range  $170 \text{ K} < T_t < 311 \text{ K}$ .  $T_t$  and  $T_C$  as well as  $\Delta T_{\text{hyst}}$  of the different samples are listed in Table 2 as well.

To study  $M_{\text{sat}}$  and the demagnetization behavior of the material states in focus of present work, field-dependent magnetization measurements were performed in PM austenite (450 K), FM austenite (300 K), and FM martensite (200, 100, and 10 K) (Figure 6). For the L-PBF sample, the target temperature of 200 K was reached by heating from lower temperatures to ensure and preserve a fully martensitic state. On the contrary, the 300 K data point was reached by cooling from higher temperatures to

maintain a fully austenitic state. Figure 6a shows  $M_{\text{sat}}$  as a function of temperature at 2 T. All samples exhibit a similar  $M_{\text{sat}}$ . The measurement error of  $\pm 5\%$  is smaller than the size of the symbols. However, a variation of  $M_{\text{sat}}$  in the range of 10% can be expected due to the slight variations in the composition of the different samples (see Table 1). Li et al.<sup>[30]</sup> reported  $M_{\text{sat}}$  of 48 and  $52 \text{ Am}^2 \text{ kg}^{-1}$  for  $\text{Co}_{50}\text{Ni}_{20}\text{Ga}_{30}$  and  $\text{Co}_{50}\text{Ni}_{22}\text{Ga}_{28}$  single crystals at 5 K, respectively. These values are in perfect agreement with the measurements for all samples probed in the present work. The DED sample exhibits the highest  $M_{\text{sat}}$  in the FM austenitic and martensitic state (300 K and below). This is in good agreement with the fact that this sample has the highest  $T_C$ . In case of the L-PBF sample,  $M_{\text{sat}}$  is affected by the Ga evaporation and the formation of  $\gamma'$ -phase at the same time (see Table 1 and

**Table 2.** Martensite and austenite start and finish temperatures  $M_S$ ,  $M_F$ ,  $A_S$ , and  $A_F$ , thermal hysteresis  $\Delta T_{\text{hyst}}$ , Curie temperature  $T_C$ , and saturation magnetization  $M_{\text{sat}}$  at 300 K for Co–Ni–Ga samples prepared by casting (as-cast), additive manufacturing using DED and L-PBF, and the Bridgman technique (single crystal).

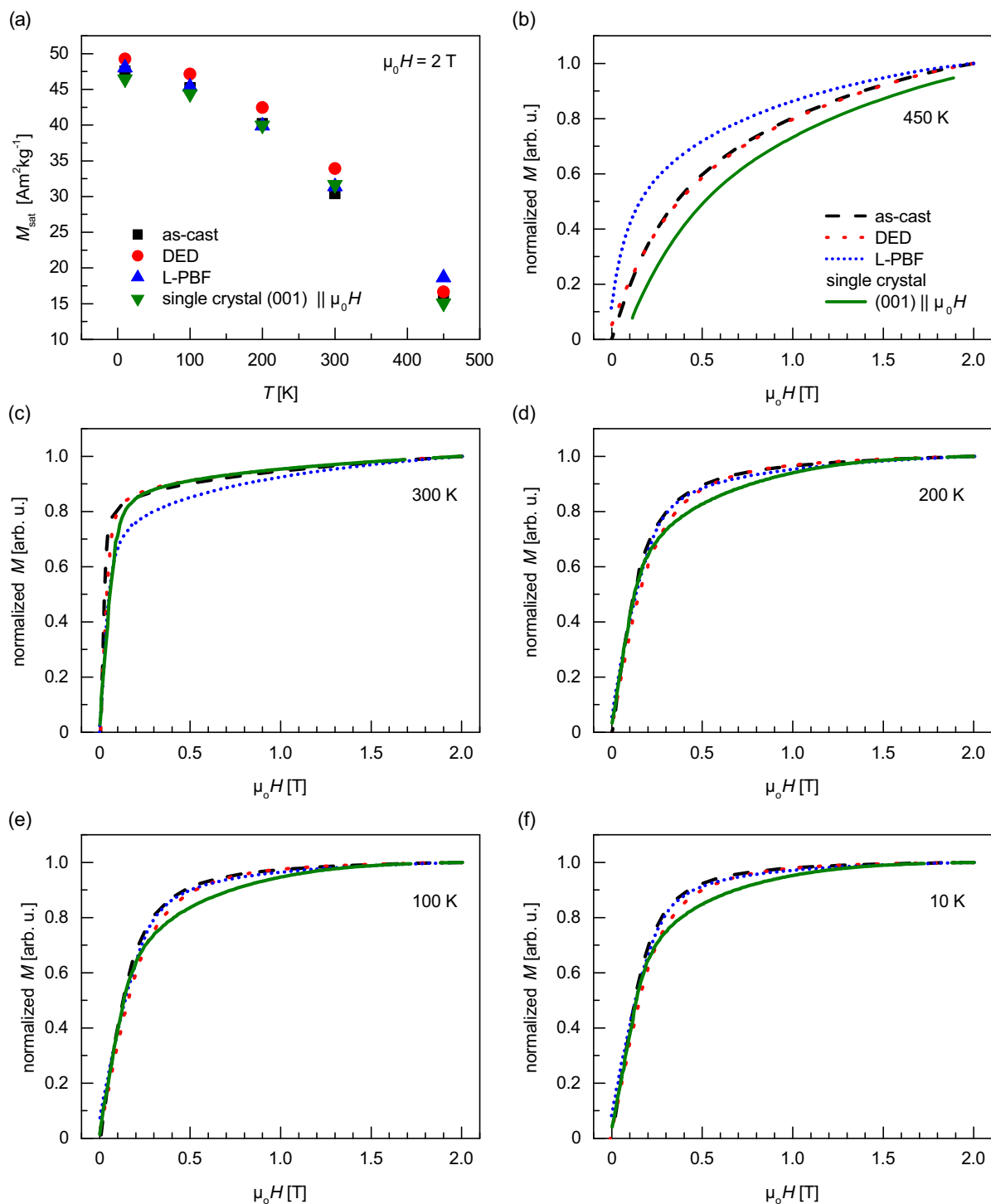
Sample	$M_S$ [K]	$M_F$ [K]	$A_S$ [K]	$A_F$ [K]	$\Delta T_{\text{hyst}}$ [K]	$T_C$ [K]	$M_{\text{sat}}$ (300 [K], 2 [T]) [Am <sup>2</sup> kg <sup>-1</sup> ]
As-cast	248	240	260	268	16	356	30.4
DED	248	244	264	275	24	397	33.9
L-PBF	268	251	279	310	39	349	31.4
Single crystal $\mu_0 H$ parallel to							
(001)	258	257	278	279	21	386	32.2
(011)	256	255	276	277	21	386	32.4
(111)	255	254	274	275	20	387	33.1

Figure 3 and 4, respectively). While Ga evaporation leads to an increase in  $M_{\text{sat}}$ , the formation of the Co-rich  $\gamma'$ -phase reduces the  $M_{\text{sat}}$  of the surrounding matrix ( $\beta$ -phase).<sup>[17]</sup> The presence of  $\gamma'$ -phase in the L-PBF sample leads to higher magnetization at 450 K compared with the other samples. At 450 K the  $\beta$ -phase is in the PM austenitic state and the magnetization of the  $\gamma'$ -phase becomes more dominant. The fact that the L-PBF sample exhibits the highest magnetization at 450 K supports the results of the microstructure analysis, that is, the sample contains a significant amount of Co-rich  $\gamma'$ -phase precipitates. This is also supported by the demagnetization curve starting from 2 T at 450 K presented in Figure 6b. All samples are in the PM austenitic state. The as-cast and DED samples and the single crystal show a very similar demagnetization curve, while the L-PBF sample reveals a higher degree of FM interaction indicated by the more pronounced drop in the demagnetization curve in small fields below 0.3 T. Figure 6c shows the demagnetization curve at 300 K, where all samples are in the FM austenitic state. In the FM state, the as-cast, DED, and single-crystalline samples exhibit a similar demagnetization behavior, while the L-PBF sample is not fully saturated at 2 T. This can be explained by the measuring temperature being close to  $T_C$  (349 K) and the presence of  $\gamma'$ -phase. Figure 6d–f shows the demagnetization curves in the FM martensitic state at 200, 100, and 10 K. Here, the as-cast, DED, and L-PBF samples exhibit the same demagnetization behavior, while the single crystal starts to demagnetize at lower fields. The latter effect can be rationalized by the single-crystalline nature of the sample.<sup>[30,52]</sup> In summary, the demagnetization behavior in the FM martensitic state is dominated by the single- and polycrystalline structure of the samples, while in the FM and PM austenitic state, the influence of the  $\gamma'$ -phase in the L-PBF-manufactured sample becomes more prominent.

For comparison,  $T_C$ ,  $T_t$  ( $M_S$ ,  $M_F$ ,  $A_S$ ,  $A_F$ ), and  $\Delta T_{\text{hyst}}$  of all samples are summarized in Figure 7a–c, respectively. A comparison of  $T_C$  (Figure 7a) shows that the as-cast material and the L-PBF sample have lower values (at  $\approx 350$  K) compared with the single-crystalline and the DED samples featuring values around 390 K. In Figure 7a,  $M_{\text{sat}}$  values of austenite (determined at 300 K and 2 T) of the individual samples are listed in red.  $T_C$ , being an intrinsic property of Co–Ni–Ga Heusler alloys, depends on

the chemical composition, magnetization, and atomic ordering.<sup>[27,30–34]</sup> The EDS measurements in Table 1 show that the DED sample and single-crystalline condition contain  $\approx 1$  at% more Co than the as-cast sample, being consistent with their higher  $T_C$  and  $M_{\text{sat}}$ . In contrast, the L-PBF sample contains the highest Co content. Therefore, one might expect the highest  $T_C$  and  $M_{\text{sat}}$  for this sample as well. However, Figure 7a shows that the L-PBF sample features the lowest  $T_C$  and only a moderate  $M_{\text{sat}}$  value, being in between that of the as-cast sample and the single crystal. With the exception of the L-PBF sample all other material conditions follow an expected trend, that is, a higher  $M_{\text{sat}}$  is associated with a higher  $T_C$ . The deviant behavior of the L-PBF sample regarding  $T_C$  and  $M_{\text{sat}}$  can be explained by the presence of the Co-rich precipitates of  $\gamma'$ -phase (Co contents of about 60 at%<sup>[40]</sup>). The formation of  $\gamma'$ -phase is known to affect the chemical composition of the surrounding austenitic matrix ( $\beta$ -phase), that is, the surrounding matrix contains less Co, eventually promoting a lower  $T_C$  of the matrix phase. As  $T_C$  of the L-PBF-processed sample is lower than  $T_C$  of the as-cast sample, it can be assumed that the Co content of the matrix ( $\beta$ -phase) could be below the Co concentration of 48.9 at% (as-cast condition). The higher  $M_{\text{sat}}$  (300 K and 2 T) of the L-PBF sample compared with the sample in as-cast condition results from the moment of the precipitates, contributing to the total magnetization. The magnetization of the  $\gamma'$ -phase leads to the FM background in the  $M(T)$  curve above  $T_C$  (Figure 5b). For the DED-processed sample, despite the fact that no subsequent heat treatment was carried out after the additive manufacturing process, the sample seems to be characterized by high  $T_C$  and  $M_{\text{sat}}$  values similar to the values provided in literature for single-crystalline material with the same composition.<sup>[27,30]</sup> The chemical inhomogeneity of the DED sample, which is highlighted in the HR-SEM BSE image in Figure 3d, seems to have no or negligible effect on the magnetic properties. This is also consistent with the absence of an FM background signal above  $T_C$ .

Figure 7b shows the FOMST temperatures  $M_S$ ,  $M_F$ ,  $A_S$ , and  $A_F$  for all material conditions investigated. Just like  $T_C$ , the FOMST temperatures are sensitive to changes in the chemical composition of the austenitic matrix ( $\beta$ -phase). Therefore, the variations in the as-cast material, the additively manufactured samples, and the single-crystalline material can be rationalized by Ga evaporation and formation of  $\gamma'$ -phase during processing. In literature, it is reported that the FOMST temperatures increase with increasing e/a ratio.<sup>[30,32,34,36–38]</sup> As the Ga evaporation during DED processing causes an increase in the Co content and, thus, an increase in the e/a ratio,<sup>[49,53]</sup> the DED sample exhibits an increase in the FOMST compared with the as-cast material. The FOMST temperatures of the single-crystalline material do not depend on the direction in case of a low applied magnetic field of 0.05 T, considering the error bar of  $\pm 2$  K (covered by the size of the symbol). The FOMST temperatures of the single crystal are about 10 K higher than in case of the as-cast material. The increase in the FOMST temperatures can be explained by a higher Co content, causing a higher e/a ratio (see Table 1). For the L-PBF sample, it has to be noted that the determination of  $M_S$ ,  $M_F$ ,  $A_S$ , and  $A_F$  using the tangent method leads to fairly large errors for  $A_S$  and  $M_F$ , as the transformation is smeared out toward lower temperatures (cf. Figure 5b). Defining the intersection of the heating and cooling curves as the finish point of the



**Figure 6.** a) Temperature-dependent saturation magnetization  $M_{\text{sat}}$  at 2 T for Co-Ni-Ga in as-cast condition, processed by DED and L-PBF and in single-crystalline state. b-f) Demagnetization curves of these samples at 450, 300, 200, 100, and 10 K.

transition, a transition width ( $|A_S - A_F|$  and  $|M_S - M_F|$ ) of more than 70 K can be read out. Still,  $A_F$  and  $M_S$  are well determinable and can be compared with those of the other samples. These values provide an increase in the FOMST temperatures in the L-PBF

state. The Ga evaporation during L-PBF processing can provide a rationale for this increase. The evaporation of Ga during processing leads to an increase in the  $e/a$  ratio, which in turn increases  $T_C$  and  $T_i$ . At the same time, it is important to note that the



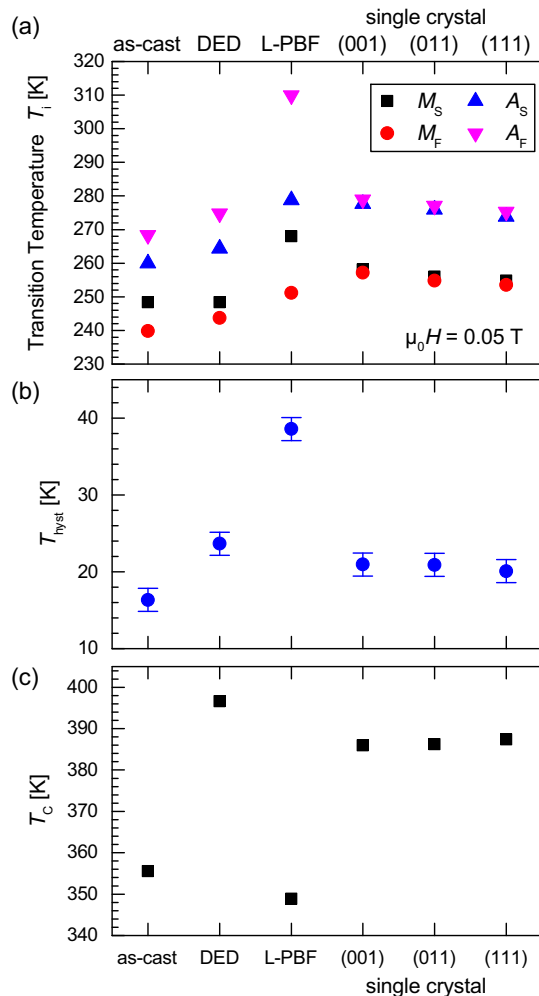


**Figure 7.** a) Curie-temperature  $T_C$ , b) transition temperatures ( $M_S$ ,  $M_F$ ,  $A_S$ ,  $A_F$ ) of the martensite and reverse martensite transformation and c) thermal hysteresis  $\Delta T_{\text{hyst}}$  of the FOMST for Co-Ni-Ga samples in as-cast condition, fabricated by DED and L-PBF and in single-crystalline state. The single-crystalline sample was probed with (001), (011) and (111) orientation parallel to the external magnetic field of 0.05 T.

formation of Co-rich precipitates ( $\gamma'$ -phase) observed in the L-PBF sample (Figure 3b and 4) reduces the Co content of the matrix ( $\beta$ -phase). The decrease in Co content leads to a decrease in  $T_C$  and  $T_t$  (see also Figure 1). Nonetheless, the influence of Ga evaporation seems to dominate, resulting in a slight overall increase in FOMST.

A broadening of the transition range after the formation of nanometric  $\gamma'$ -phase precipitates was observed in Co-Ni-Ga single crystals after aging at 650 K.<sup>[39,49,53]</sup> Hereby, the precipitates can lead to pinning-induced stabilization of martensite and increase in interfacial friction.<sup>[54,55]</sup>

The pinning explains the large transformation width of the martensite ( $M_S$ - $M_F$ ) and reverse martensite ( $A_S$ - $A_F$ ) transformation of more than 30 K for the L-PBF sample. In contrast, the single crystal exhibits a sudden FOMST, and the full transformation takes place between two measurement points (step size 1 K,

see Figure 5a). The polycrystalline as-cast material and the textured DED sample transform within a temperature interval of about 8 K. The increase in the transition width compared with the single crystal can be explained by constraints of the grain boundaries and defects; however, the effect is less pronounced as in the L-PBF sample.

Figure 7c shows  $\Delta T_{\text{hyst}}$  of the FOMST for different samples.  $\Delta T_{\text{hyst}}$  depends on phenomena related to grain boundaries and defects, but also on the chemical composition, the magnetic anisotropy, and  $T_t$ .<sup>[28,29,56]</sup> The Co-Ni-Ga single-crystalline material and the DED-manufactured sample exhibit a  $\Delta T_{\text{hyst}}$  of about 22 K ( $\pm 2$  K), while the as-cast material shows a lower  $\Delta T_{\text{hyst}}$  of 16 K. These samples differ significantly in grain size and orientation: micrometer-sized textured grains in the DED sample, millimeter-sized random oriented grains in the as-cast sample, and a single grain in centimeter size in case of the single crystal. With respect to the composition, it has to be emphasized that the as-cast sample has a lower Co content than the other two samples. This indicates that grain size and orientation play a minor role in these samples, while a higher Co content seems to increase  $\Delta T_{\text{hyst}}$ . The significant increase in  $\Delta T_{\text{hyst}}$  in the L-PBF sample and the broadened phase transition range can be explained by the presence  $\gamma'$ -phase.<sup>[49]</sup>

The comparison of the magnetic properties of all investigated samples shows that the DED-manufactured sample reveals characteristics being comparable with the single crystal, while the L-PBF sample is characterized by a strong broadening of the transition temperatures due to the formation of  $\gamma'$ -precipitates. Furthermore, the presence of  $\gamma'$ -precipitates can easily be detected by measuring the FM background in the  $M(T)$  curve above  $T_C$  (Figure 5b). This analysis method is simple and less time-consuming than microstructural analysis using HR-SEM or TEM and, thus, can be used for screening of larger sample quantities for optimized transformation properties.

## 4. Conclusion

In this study, the influence of the processing method and microstructure on FOMST in Heusler Co-Ni-Ga FMSMA was investigated. The main results can be summarized as follows: 1) Microstructural HR-SEM and TEM analysis reveals the presence of Co-rich  $\gamma'$ -phase in the L-PBF-processed sample. The Co-rich  $\gamma'$ -phase leads to a FM background above the Curie temperature of the matrix ( $\beta$ -phase). Most importantly, the  $\gamma'$ -precipitates affect the FOMST, that is, cause a drastic increase of the transition width and  $\Delta T_{\text{hyst}}$  compared with single-crystalline material as well as polycrystalline samples in the as-cast and DED-processed state. 2) In case of the DED-processed sample, HR-SEM analysis reveals no evidence of significant amounts of  $\gamma'$ -phase, but a slight elongated chemical inhomogeneity along the BD. This inhomogeneity has a minor or even no effect on the FOMST, as the DED sample exhibits similar values for  $T_t$ ,  $\Delta T_{\text{hyst}}$ , and  $T_C$  as the single crystal. 3) The transition behavior of the DED-processed material is similar to that of its single-crystalline counterpart, making additively manufactured Co-Ni-Ga using DED a promising alternative for single crystals in FMSMA applications. It is expected that the DED technique will be suitable to tailor the grain structure in

other FMSMAs as well, for example, Ni–Mn-based Heusler alloys, improving their mechanical stability for elastocaloric or multicaloric applications.

## Acknowledgements

This work was supported by funding from the European Research Council (ERC) under the European Union's Horizon 2020 research and innovation program (grant number. 743116, Cool Innov), the Deutsche Forschungsgemeinschaft SPP 1599, and CRC/TRR 270 "HoMMage" Project-ID 405553726-TRR 270. T.N. acknowledges funding by DFG (grant number 456078747). The authors gratefully acknowledge the assistance of Julia Richter, Moritz Kahlert, Michael Wiegand, Niklas Sommer, and Gabriel Mienert with the fabrication via the additive manufacturing techniques.

Open Access funding enabled and organized by Projekt DEAL.

## Conflict of Interest

The authors declare no conflict of interest.

## Data Availability Statement

The data that support the findings of this study are available from the corresponding author upon reasonable request.

## Keywords

additive manufacturing, direct microstructure designs, first-order magnetostructural transitions, magnetic characterizations, shape memory alloys

Received: January 14, 2022

Revised: February 25, 2022

Published online: March 28, 2022

- [1] J. Pons, E. Cesari, C. Segui, F. Masdeu, R. Santamarta, *Mater. Sci. Eng. A* **2008**, 481–482, 57.
- [2] A. Sozinov, A. A. Likhachev, K. Ullakko, *IEEE Trans. Magn.* **2002**, 38, 2814.
- [3] V. A. Chernenko, S. Besseghini, *Sens. Actuators Phys.* **2008**, 142, 542.
- [4] K. Ullakko, J. K. Huang, C. Kantner, R. C. O'Handley, V. V. Kokorin, *Appl. Phys. Lett.* **1996**, 69, 1966.
- [5] A. Fujita, K. Fukamichi, F. Gejima, R. Kainuma, K. Ishida, *Appl. Phys. Lett.* **2000**, 77, 3054.
- [6] H. E. Karaca, I. Karaman, B. Basaran, Y. Ren, Y. I. Chumlyakov, H. J. Maier, *Adv. Funct. Mater.* **2009**, 19, 983.
- [7] L. Mañosa, X. Moya, A. Planes, S. Aksoy, M. Acet, E. F. Wassermann, T. Krenke, *Mater. Sci. Forum.* **2008**, 583, 111.
- [8] M. Acet, L. Manosa, A. Planes, *Handbook of Magnetic Materials*, Vol. 19, Elsevier B.V., Oxford **2011**.
- [9] N. M. Bruno, I. Karaman, Y. I. Chumlyakov, *Phys. Status Solidi B* **2018**, 255, 1700437.
- [10] K. Oikawa, L. Wulff, T. Iijima, F. Gejima, T. Ohmori, A. Fujita, K. Fukamichi, R. Kainuma, K. Ishida, *Appl. Phys. Lett.* **2001**, 79, 3290.
- [11] J. Dadda, D. Canadinc, H. J. Maier, I. Karaman, H. E. Karaca, Y. I. Chumlyakov, *Philos. Mag.* **2007**, 87, 2313.
- [12] P. Krooß, T. Niendorf, P. M. Kadletz, C. Somsen, M. J. Guann, Y. I. Chumlyakov, W. W. Schmahl, G. Eggeler, H. J. Maier, *Shape Mem. Superelasticity* **2015**, 1, 6.
- [13] A. Reul, C. Lauhoff, P. Krooß, M. J. Guann, P. M. Kadletz, Y. I. Chumlyakov, T. Niendorf, W. W. Schmahl, *Shape Mem. Superelasticity* **2018**, 4, 61.
- [14] C. Lauhoff, M. Vollmer, P. Krooß, I. Kireeva, Y. I. Chumlyakov, T. Niendorf, *Shape Mem. Superelasticity* **2019**, 5, 73.
- [15] M. Vollmer, P. Krooß, C. Segel, A. Weidner, A. Paulsen, J. Frenzel, M. Schaper, G. Eggeler, H. J. Maier, T. Niendorf, *J. Alloys Compd.* **2015**, 633, 288.
- [16] R. D. Dar, H. Yan, Y. Chen, *Scr. Mater.* **2016**, 115, 113.
- [17] K. Prusik, H. Morawiec, B. Kostrubiec, M. Prewendowski, G. Dercz, K. Ziewiec, *Eur. Phys. J. Spec. Top.* **2008**, 158, 155.
- [18] M. Sato, T. Okazaki, Y. Furuya, M. Wuttig, *Mater. Trans.* **2003**, 44, 372.
- [19] J.-L. Liu, H.-Y. Huang, J.-X. Xie, *Mater. Des.* **2014**, 64, 427.
- [20] S. M. Ueland, Y. Chen, C. A. Schuh, *Adv. Funct. Mater.* **2012**, 22, 2094.
- [21] J.-L. Liu, H.-Y. Huang, J.-X. Xie, S. Xu, F. Li, *Scr. Mater.* **2017**, 136, 106.
- [22] C. Lauhoff, A. Fischer, C. Sobrero, A. Liehr, P. Krooß, F. Brenne, J. Richter, M. Kahlert, S. Böhm, T. Niendorf, *Metall. Mater. Trans. A* **2020**, 51, 1056.
- [23] C. Lauhoff, N. Sommer, M. Vollmer, G. Mienert, P. Krooß, S. Böhm, T. Niendorf, *Mater. Res. Lett.* **2020**, 8, 314.
- [24] T. Niendorf, S. Leuders, A. Riemer, F. Brenne, T. Tröster, H. A. Richard, D. Schwarze, *Adv. Eng. Mater.* **2014**, 16, 857.
- [25] L. Thijs, K. Kempen, J.-P. Kruth, J. Van Humbeeck, *Acta Mater.* **2013**, 61, 1809.
- [26] L. Thijs, M. L. Montero Sistiaga, R. Wauthle, Q. Xie, J.-P. Kruth, J. Van Humbeeck, *Acta Mater.* **2013**, 61, 4657.
- [27] K. Oikawa, T. Ota, F. Gejima, T. Ohmori, R. Kainuma, K. Ishida, *Mater. Trans.* **2001**, 42, 2472.
- [28] O. Gutfleisch, T. Gottschall, M. Fries, D. Benke, I. Radulov, K. P. Skokov, H. Wende, M. Gruner, M. Acet, P. Entel, M. Farle, *Eng. Sci.* **2016**, 374, 20150308.
- [29] F. Scheibel, T. Gottschall, A. Taubel, M. Fries, K. P. Skokov, A. Terwey, W. Keune, K. Ollefs, H. Wende, M. Farle, M. Acet, O. Gutfleisch, M. E. Gruner, *Energy Technol.* **2018**, 6, 1397.
- [30] Y. X. Li, H. Y. Liu, F. B. Meng, L. Q. Yan, G. D. Liu, X. F. Dai, M. Zhang, Z. H. Liu, J. L. Chen, G. H. Wu, *Appl. Phys. Lett.* **2004**, 84, 3594.
- [31] N. Singh, E. Dogan, I. Karaman, R. Arróyave, *Phys. Rev. B* **2011**, 84, 184201.
- [32] E. Dogan, I. Karaman, N. Singh, A. Chivukula, H. S. Thawabi, R. Arroyave, *Acta Mater.* **2012**, 60, 3545.
- [33] P. M. Kadletz, P. Krooß, Y. I. Chumlyakov, M. J. Guann, W. W. Schmahl, H. J. Maier, T. Niendorf, *Mater. Lett.* **2015**, 159, 16.
- [34] J. Liu, H. Zheng, M. Xia, Y. Huang, J. Li, *Scr. Mater.* **2005**, 52, 935.
- [35] K. Otsuka, X. Ren, *Mater. Sci. Eng. A* **2001**, 312, 207.
- [36] C. Craciunescu, Y. Kishi, T. A. Lograsso, M. Wuttig, *Scr. Mater.* **2002**, 47, 285.
- [37] A. Tejada-Cruz, F. Alvarado-Hernández, D. E. Soto-Parra, R. Ochoa-Gamboa, P. O. Castillo-Villa, *J. Alloys Compd.* **2010**, 499, 183.
- [38] K. Oikawa, T. Ota, Y. Imano, T. Omori, R. Kainuma, K. Ishida, *J. Phase Equilibria Diffus.* **2006**, 27, 75.
- [39] C. Lauhoff, A. Reul, D. Langenkämper, P. Krooß, C. Somsen, M. J. Guann, I. Kireeva, Y. I. Chumlyakov, W. W. Schmahl, T. Niendorf, *Scr. Mater.* **2019**, 168, 42.
- [40] E. Dogan, I. Karaman, Y. I. Chumlyakov, Z. P. Luo, *Acta Mater.* **2011**, 59, 1168.
- [41] H. Kalaantari, S. Amini, J. Hong, R. Abbaschian, *J. Mater. Sci.* **2011**, 46, 6224.

- [42] Y. I. Chumlyakov, I. V. Kireeva, E. Y. Panchenko, E. E. Timofeeva, Z. V. Pobedennaya, S. V. Chusov, I. Karaman, H. Maier, E. Cesari, V. A. Kirillov, *Russ. Phys. J.* **2008**, 51, 1016.
- [43] C. Lauhoff, A. Reul, D. Langenkämper, P. Krooß, C. Somsen, M. J. Guann, B. Pedersen, I. Kireeva, Y. I. Chumlyakov, G. Eggeler, W. W. Schmahl, T. Niendorf, *Acta Mater.* **2022**, 226, 117623.
- [44] C. Sobrero, J. Basbus, C. Lauhoff, M. Etter, A. Liehr, T. Niendorf, *Funct. Mater. Lett.* **2021**, 2250007, <https://doi.org/10.1142/S1793604722500072>.
- [45] J. Dadda, H. J. Maier, I. Karaman, H. E. Karaca, Y. I. Chumlyakov, *Scr. Mater.* **2006**, 55, 663.
- [46] N. Sommer, G. Mienert, M. Vollmer, C. Lauhoff, P. Krooß, T. Niendorf, S. Böhm, *Adv. Mater. Res.* **2021**, 1161, 105.
- [47] M. E. Glicksman, *Principles of solidification: An introduction to modern casting and crystal growth concepts*, Springer, New York, **2011**.
- [48] J. Liu, H. Xie, Y. Huo, H. Zheng, J. Li, *J. Alloys Compd.* **2006**, 420, 145.
- [49] I. V. Kireeva, J. Pons, C. Picornell, Y. I. Chumlyakov, E. Cesari, I. V. Kretinina, *Intermetallics* **2013**, 35, 60.
- [50] DIN SPEC 91373:2018-06, Magnetokalorik- Terminologie; Text Englisch, Beuth Verlag GmbH, n.d. <https://www.beuth.de/de/-/-/288638546> (accessed January 4, 2022).
- [51] A. Taubel, T. Gottschall, M. Fries, S. Riegg, C. Soon, K. P. Skokov, O. Gutfleisch, *Phys. Status Solidi B* **2018**, 255, 1700331.
- [52] H. Morito, K. Oikawa, A. Fujita, K. Fukamichi, R. Kainuma, K. Ishida, *J. Phys. Condens. Matter.* **2009**, 21, 256002.
- [53] I. V. Kireeva, C. Picornell, J. Pons, I. V. Kretinina, Y. I. Chumlyakov, E. Cesari, *Acta Mater.* **2014**, 68, 127.
- [54] S. Kustov, J. Pons, E. Cesari, J. Van Humbeeck, *Acta Mater.* **2004**, 52, 3083.
- [55] J. Dadda, H. J-rgen Maier, I. Karaman, Y. Chumlyakov, *Int. J. Mater. Res.* **2010**, 101, 1.
- [56] H. Sepehri-Amin, A. Taubel, T. Ohkubo, K. P. Skokov, O. Gutfleisch, K. Hono, *Acta Mater.* **2018**, 147, 342.